Research Article | Vol. 32, No. 20 / 23 Sep 2024 / Optics Express 35551
Optics EXPRESS

On-chip broadband Mach-Zehnder interferometer based on a broadband taper-section phase shifter

XIHENG AI,[1] YANG ZHANG,[1] WEI-LUN HSU,[1] SYLVAIN VEILLEUX,[2] AND MARIO DAGENAIS[1,*]

[1]Department of Electrical and Computer Engineering, University of Maryland, College Park, MD 20770, USA
[2]Department of Astronomy, University of Maryland, College Park, MD 20770, USA
[*]dage@umd.edu

Abstract: In this paper, we propose a new broadband nulling interferometer based on the Si_3N_4/SiO_2 platform which utilizes a π-phase shifter. This π-phase shift multimode interference Mach-Zehnder interferometer (πPS MMI-MZI) leverages a novel low phase shift error (PSE) and broadband taper-section phase shifter (TSPS). For the TSPS, our simulation predicts an unprecedented PSE from 1450 nm to 1650 nm for the two- and three-section TSPS of 1^o and 0.02^o, respectively. Our experimental results demonstrate a PSE of 1^o within a 190 nm bandwidth for the two-section TSPS. A slightly adjusted TSPS gives an even lower PSE of 0.6^o within a narrower bandwidth of 90 nm. With the help of the TSPS, the πPS MMI-MZI shows a significant improvement in extinction ratio compared to the conventional MMI-MZI. Simulations predict an extinction ratio of 50 dB within a 150 nm bandwidth. Experimental measurements demonstrate a 40 dB extinction ratio within a 100 nm bandwidth. The broadband TSPS, as well as the broadband πPS MMI-MZI, pave the way for novel high performance photonic integrated circuits.

1. Introduction

On-chip high performance Mach-Zehnder interferometers (MZI) have attracted much interest in photonics applications. Nulling interferometers based on MZIs have been used to detect exoplanets in astrophysics [1,2]. In programmable optical circuits, MZIs are used as optical switches to change the optical routing [3–6]. In quantum computation, MZI can be used for qubits manipulation [7,8]. Among these applications, the extinction ratio of the MZI is the most important factor. Due to fabrication imperfections, the beam splitter in a MZI, either a directional coupler or a multimode interference coupler, will suffer a power imbalance and phase inaccuracy. In a multistage approach, two tunable MZIs are optimized separately then connected to reach a high extinction ratio [8–10]. However, this method increases the control complexity and power loss due to the extra beam splitters and phase shifters involved.

In addition, the working bandwidth of the MZI is also important for nearly all the applications mentioned above. The bandwidth of the MZIs is limited by that of the beam splitters as well as by the active phase shifters used to fine tune the phase [11]. In this paper, we propose a passive π-phase shifter MZI solution based on an ideal broadband phase shifter (see Fig. 1). Both the power imbalance and the phase inaccuracy caused by the imperfection and bandwidth limitation of the beam splitters can be compensated by a phase flip in the MZI arms.

Optical Phase shifters (PSs) are key components in integrated photonics. They are used in optical modulators [12], mode (de)multiplexers [13,14], switches [15,16], and tunable filters [17,18]. The optical path length differences between the signals can be engineered using either active or passive designs in integrated photonics. Active PSs utilizing the thermo-optical effect [19], electro-mechanical effect [20,21], nonlinear optical effect [21] and resonators [22,23] have

#531698 https://doi.org/10.1364/OE.531698
Journal © 2024 Received 24 Jun 2024; revised 8 Aug 2024; accepted 27 Aug 2024; published 18 Sep 2024

Optics EXPRESS

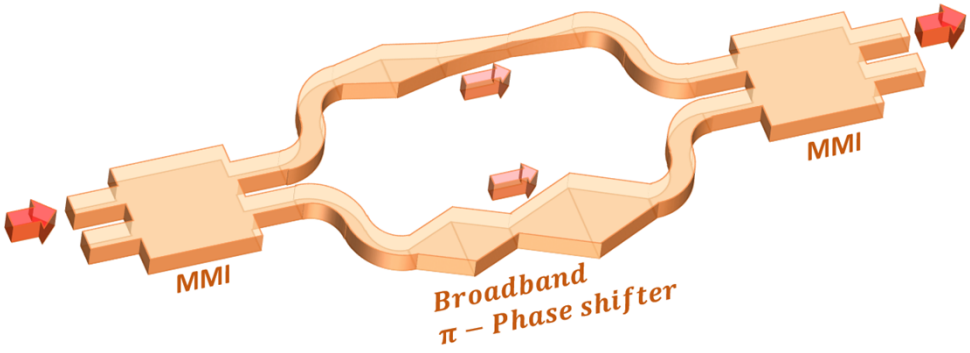

Fig. 1. schematic modal of the πPS MMI-MZI consisting of two MMI couplers and a novel broadband π-phase shifter.

previously been reported. Passive PSs are preferred in the case where power consumption is restricted. Without the limitations of driving power and control complexity, passive PSs are suitable for many applications. Besides the typically used adiabatic taper PSs [24] and dissimilar length PSs [25,26], PSs based on a 1×1 MMI couplers [27]and tilted joint MMI PSs [28] have also been reported.

The bandwidth and the phase accuracy of the PSs need to be significantly improved for the next generation of photonic devices. This also applies to the π-PS MZI we propose in this paper. Relevant to this goal, a broadband 90° subwavelength grating (SWG) PS has been proposed, with a phase shift error (PSE) less than 3° within a 145 nm bandwidth [29]. Pushing forward, we propose an innovative integrated tapered-section phase shifter (TSPS) based on a multi-section PS structure. The theory of this multi-section PS design is discussed in [30]. Using the effective refractive indices (RI) of the tapers, we further decrease the complexity and the length of the multi-section PSs. Our design is based on the silicon nitride platform. The simulation shows a 1°/0.02° PSE within a 200 nm bandwidth for the two/three-section TSPS design, respectively. We optimized the two-section TSPS experimentally, reaching an unprecedented PSE of 1° from 1450 nm to 1640 nm. We note that the PSE of our PSs should be lower for a phase shift smaller than 180°, since the PSE of a PS is proportional to its total phase shift. In addition, we demonstrated an adjusted TSPS with an even smaller PSE of 0.6° within a narrower bandwidth of 90 nm around 1550 nm for the applications requiring a stricter phase control.

Utilizing the TSPS, the simulation result of the πPS MMI-MZI shows a high extinction ratio of 50 dB within a 150 nm bandwidth. The experimental result presents an extinction ratio of 40 dB within a 100 nm bandwidth, indicating a significant improvement compared to the conventional MMI-MZI which shows an extinction ratio of 30 dB within a 90 nm bandwidth [11].

The low-PSE broadband TSPS as well as the broadband πPS MMI-MZI provide high-performance building blocks for integrated photonics. These technical advancements will not only improve the performance of the devices based on phase shift and interference nulling, but also will provide powerful components for the next generation of optical devices.

2. Principles

2.1. Broadband Mach-Zehnder interferometer

2.1.1. Traditional on-chip MZI based on MMI

A conventional MMI-MZI is a MZI formed by two cascaded MMIs (see Fig. 2). Assuming a single mode is injected from port 1, an MMI coupler will split the input power equally between ports 3 and 4 within a certain bandwidth. The phase difference between the modes coming from these

Optics EXPRESS

two ports should be $\pi/2$. After propagating along the two arms connecting the cascaded MMI couplers, the phase mismatch between ports 5 and 6 should remain $\pi/2$. Similar power splitting process repeats at the second MMI coupler for both input ports 5 and 6. Consequentially, the two signals coming out from port 8 (bright port) have the same phase and they will constructively interfere, so most of the energy will come out from port 8. On the other hand, the two signals coming out from port 7 (dark port) have a π-phase difference and they will destructively interfere so that barely any energy comes out. The energy ratio between port 8 and port 7 is called the extinction ratio.

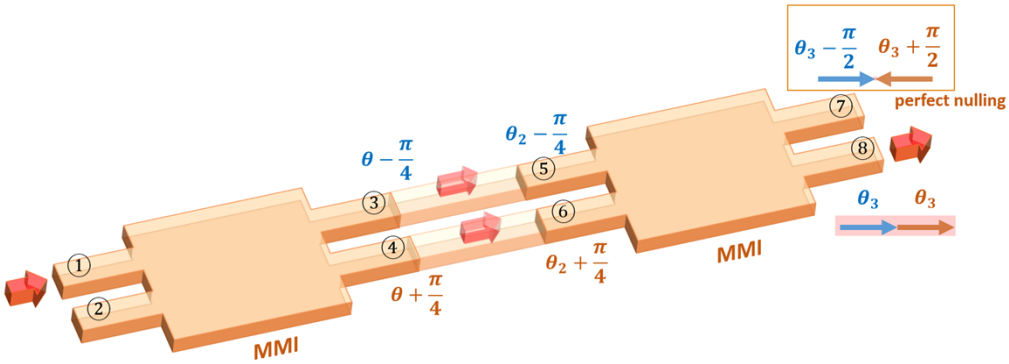

Fig. 2. schematic model of a MMI-MZI. In the first MMI coupler, the input mode at port 1 splits into two modes (in blue and red color) with a phase difference of $\pi/2$. Those two modes undergo a power splitting in the second MMI coupler, respectively. The phase information in blue at port 7 and port 8 corresponds to the two modes split from the mode coming from port 3. Similarly, the two modes in red at port 7 and port 8 originates from the mode at port 4. The destructive interference at port 7 gives a perfect nulling.

2.1.2. Broadband MZI with a π-phase shifter

The performance of the conventional MMI-MZI is limited by the performance of the MMI couplers. Based on the self-imaging principle [31], a MMI coupler can only work perfectly for its center wavelength. Both the power-imbalance of the two output ports and the phase accuracy will suffer when the device is not operated under the center wavelength or when the design/fabrication is not optimized. Here, we discuss the relationship between the extinction ratio and the MMI coupler performance.

First, we investigate the MZI's imperfect nulling brought by the MMI power-imbalance. Instead of perfectly splitting 50%/50% the original input power, we assume that the power coming from ports 3 and 4 are α and β. Here α, β<50% and $\alpha \neq \beta$ (Fig. 3(a)). Both α and β are below 50% because of light scattering [32]. We repeat the power splitting at the second MMI coupler and we get a total of four signals at the output ports. The power outputs of the two signals at port 7 are α^2 (power α at port 5 splits to α^2 and $\alpha\beta$ at port 7 and 8, shown in blue color) and β^2 (power β at port 6 splits to β^2 and $\beta\alpha$ at port 7 and 8, shown in red color) separately, so their amplitude should be α and β. Since they are not equal to each other, the nulling interference is not perfect.

Then we investigate the relationship between the extinction ratio and the phase accuracy (Fig. 3(b)). Now we assume that the phase difference between the two MMI coupler outputs is not perfectly $\pi/2$. For convenience we set the phase of port 3 and port 4 to be $\Delta\theta - \frac{\pi}{4}$ and $\frac{\pi}{4}$.

After repeating the power splitting at the second MMI coupler, the resulting phase difference is still zero for the two signals at port 8. This leads to constructive interference at port 8. However, the phases of the two signals at port 7 are now $2\Delta\theta - \frac{\pi}{2}$ and $\frac{\pi}{2}$ so their phase difference is $\pi - 2\Delta\theta$. These two modes cannot perfectly cancel out each other because of this $2\Delta\theta$ phase error. The

Optics EXPRESS

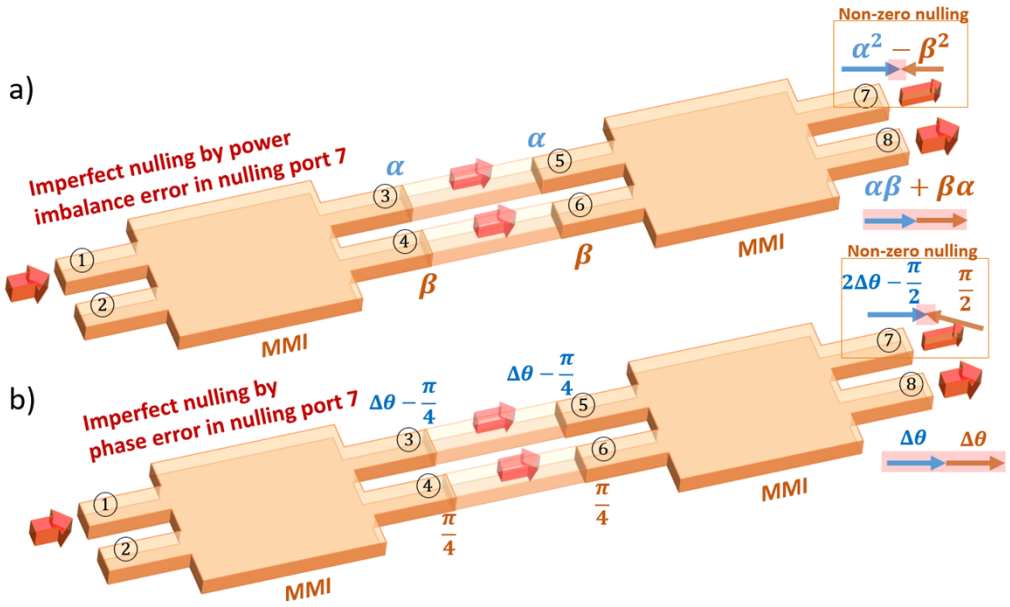

Fig. 3. a) imperfect nulling brought by MMI power imbalance (α>β). There is power remaining at port 7 after destructive interference. b) Imperfect nulling brought by MMI phase inaccuracy. The modes interfering with each other at port 7 do not have a phase difference of π accurately.

power imbalance and phase inaccuracy of the MMI make the destructive interference imperfect. There is still a certain amount of power coming out from the nulling port, which results in the performance and bandwidth limitation of the MMI-MZI device as a nulling interferometer.

As a simple solution, here we propose an innovative way to compensate the imperfection brought by the MMI couplers by adding a π-phase shifter (πPS) between the two cascaded MMI couplers (Fig. 4). Now the phase of the mode in port 4 can be flipped by 180°, compared to port 3. The phase in brown color in Fig. 4(b) should all be flipped by 180°. Consequently, destructive interference happens at port 8 now while constructive interference happens at port 7. This time the phases of two signals at port 8 are $\Delta\theta$ and $\Delta\theta - \pi$. The phase difference is exactly π so the nulling can be perfect.

When we go from a standard MZI to a πPS-MZI, the dark port moves from port 7 to port 8 and the energies of the two signals at the output are given by $\alpha\beta$ and $\beta\alpha$ (Fig. 4(a)), which are identical. So the amplitudes of the two modes are also the same, which gives a perfect nulling even in the presence of an MMI power-imbalance.

In conclusion, adding a πPS can solve both the power imbalance and the phase inaccuracy problem from the MMI imperfection/bandwidth limitation. Two MMI couplers now compensate each other to reach a perfect nulling.

2.2. *Integrated broadband phase shifter*

A key element in the proposed design is the πPS which should have a low phase shift error (PSE) for a wide bandwidth. Since the phase error of an MMI coupler is about $\Delta\theta \sim 1°$, the PSE of the PS should be smaller than $2\Delta\theta \sim 2°$ for the entire operating bandwidth in order to compensate the phase inaccuracy.

Since such a high performance on-chip PS has not been reported yet, we have to design our own low PSE broadband PS. We further develop the theory in [30] to transform it from the fiber

Optics EXPRESS

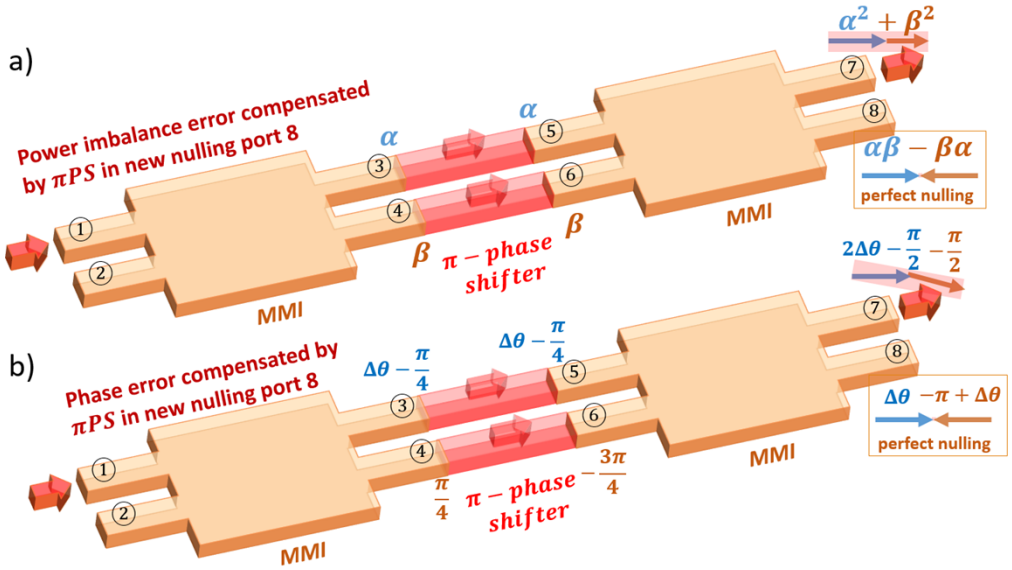

Fig. 4. a) Compensation for MMI power imbalance using a πPS. With the help of the πPS, the destructive interference happens at port 8, where the amplitudes of the two interfering modes are the same b) Compensation for MMI phase inaccuracy using a πPS. At port 8, the phase difference between two modes is exactly π.

system to the integrated optics platform. The original sectioned phase shifter (SPS) theory was worked out by P. Labeye in his thesis [33].

Based on the sectioned PS design, the length of the PS can be several millimeters to one centimeter, which can be easily used in a fiber system but is harder to implement on an optical chip. Besides the pattern layout challenges brought by the large footprint, a long PS may also cause directional coupling between the two arms. To solve these problems, we propose an innovative on-chip taper-section phase shifter design to decrease the length of the device.

The traditional PS uses two ways to create a phase difference. The first is to add an extra length to one of the two arms. Their optical path difference can be designed to reach a desired phase difference. However the routing of the two arms with different lengths may be challenging. A preferred way is to use two waveguide arms with the same length but different widths, so their effective refractive indices are different. As a result of this, the optical lengths for the two arms can be different and can create a phase difference.

However, both methods have narrow bandwidths because the phase difference $\Delta\phi = \Delta L/\lambda$ (where ΔL is the optical length difference and λ is the wavelength) depends on the length difference and the optical wavelength. For the extra length phase shifting method, the same optical length difference ΔL will result in a different phase shift $\Delta\phi$ for different wavelengths. Moreover, in the case of the second method, the effective RI of the waveguides has a dependence on wavelength, making the phase also dependent on the wavelength.

Now we explain how the SPS can remove the wavelength dependence by first considering a two-section phase shifter design. In Fig. 5, two parallel waveguides with widths W_1 and W_2 are connected with two waveguides with widths W_3 and W_4, respectively. For length l_1, the effective RI difference $\Delta n_1(\lambda)$ between the two waveguides with widths W_1 and W_2 can be expanded as polynomials: $\Delta n_1(\lambda) = A_1 + B_1\lambda + C_1\lambda^2 + \ldots$

Optics EXPRESS

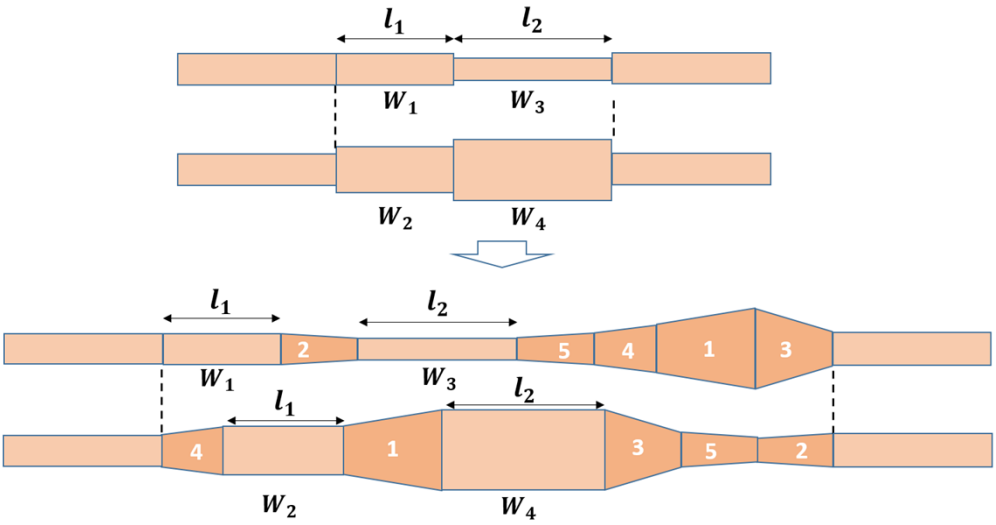

Fig. 5. Multi-section PS and the taper design. The tapers are used to avoid the mode mismatch loss between the waveguide sections. Each of the tapers in one PS arm can find its counterpart in the other arm so there is no extra phase difference introduced by adding the tapers.

Here we expand it to first order in λ. So $\Delta n_1(\lambda) \approx A_1 + B_1\lambda$ and for length l_2, $\Delta n_2(\lambda)$ between W_3 and W_4 can be written as: $\Delta n_2(\lambda) \approx A_2 + B_2\lambda$. So the total phase shift

$$\frac{\theta(\lambda)}{2\pi} = \frac{\Delta n_1(\lambda)}{\lambda} l_1 + \frac{\Delta n_2(\lambda)}{\lambda} l_2 \approx \left(\frac{A_1}{\lambda} + B_1\right) l_1 + \left(\frac{A_2}{\lambda} + B_2\right) l_2 = \frac{(A_1 l_1 + A_2 l_2)}{\lambda} + (B_1 l_1 + B_2 l_2) \tag{1}$$

If we design the length ratio to be $\frac{l_1}{l_2} = -\frac{A_2}{A_1}$ then $\frac{(A_1 l_1 + A_2 l_2)}{\lambda} = 0$. The remaining term will be independent of wavelength: $\frac{\theta(\lambda)}{2\pi} = B_1 l_1 + B_2 l_2 = \frac{\theta_0}{2\pi}$. Now we can multiply l_1 and l_2 by the same factor to reach any phase shift we want.

Similarly, a three-section phase shifter supports a second order polynomial. In this case,

$$\frac{\theta(\lambda)}{2\pi} = \frac{1}{\lambda} \sum\nolimits_{i=1,2,3} (A_i + B_i\lambda + C_i\lambda^2) l_i \quad = \frac{1}{\lambda} \sum\nolimits_{i=1,2,3} (A_i + C_i\lambda^2) l_i + \sum\nolimits_{i=1,2,3} B_i l_i \tag{2}$$

For a desired constant phase shift θ_0, the length l_1, l_2, l_3 can be solved by the matrix calculation:

$$\begin{bmatrix} A_1 & A_2 & A_3 \\ B_1 & B_2 & B_3 \\ C_1 & C_2 & C_3 \end{bmatrix} \cdot \begin{bmatrix} l_1 \\ l_2 \\ l_3 \end{bmatrix} = \begin{bmatrix} 0 \\ \theta_0/2\pi \\ 0 \end{bmatrix} \tag{3}$$

Between the different waveguide sections, tapers should be used to avoid energy loss caused by mode mismatch. Also, to compensate the phase shift introduced by the tapers, each taper should find its copy in the other arm. Using the two-section case as an example (see Fig. 5), taper #2 is used to connect waveguide W_1 and W_3. We can find its counterpart in the bottom arm. Similarly taper #1 used to connect waveguide W_2 and W_4 can find its counterpart in the top arm. The phase difference between the two arms will not change after the tapers are added between the sections.

To avoid power loss in the SPS, the length of the tapers should be long enough. As a result, the total length of the three-section design can be more than a centimeter while a two-section

Optics EXPRESS

design can be several millimeters. The large footprint of the SPS makes it hard to be integrated in on-chip optical circuits. In addition, a long device makes directional coupling easier to happen between the arms and the larger total optical length makes phase control harder.

To address this footprint problem, we propose a new taper-section phase shifter (TSPS) design. For a linear taper, the effective RI is different at different positions because the width of the waveguide is different (see Fig. 6(a)). However when we extend the taper linearly by a factor, the optical length of the whole taper should enlarge by the same factor because each infinite short section that has a local effective RI_i will be extended by that same factor. For example, if a taper with length l_0 gives a θ_0 phase shift, it should give a $2\theta_0$ phase shift if we extend its length to $2l_0$ linearly. Now we can define an effective RI for a linear taper to be $n_{\text{taper}}(\lambda) = \left(\frac{\theta_0}{l_0}\right)\frac{\lambda}{2\pi} = \left(\frac{2\theta_0}{2l_0}\right)\frac{\lambda}{2\pi}$

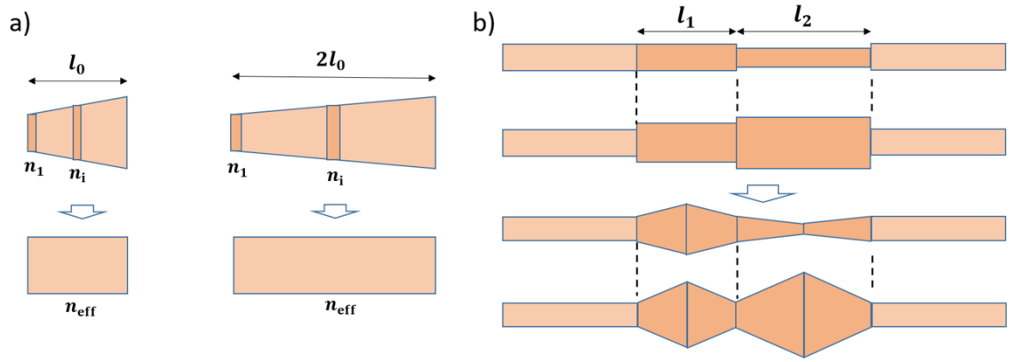

Fig. 6. a) A taper can be treated as a straight waveguide with the effective RI in terms of phase shift. b) TSPS design by substituting straight waveguides by taper sections which can be connected directly. Compared to Fig. 5, the tapers themselves create the phase shift, the total device length can be shorter.

Based on this, now we can use the tapers themselves to act as a PS so we do not need extra tapers to connect them. We set the width of one taper end to be a constant W_0 which applies to all the taper sections. Then we can vary the width W_i on the other end to get different n_{taper}. A pair of same tapers connected by the taper end with width W_i to form a taper section. Each section can be connected to each other directly because the width of their ends should all be W_0 (see Fig. 6(b)).

Now we follow a similar process discussed in the SPS but use n_{taper} of each taper section instead of the RI of straight waveguides. The complexity and the length of the SPS can be significantly reduced while the performance can remain the same.

3. Simulations

3.1. Design and simulation of the broadband phase shifter

Considering a 300 nm thick silicon nitride (Si_3N_4) platform with silicon dioxide (SiO_2) cladding, the "connection width" W_0 is set to be 1um so the waveguides support only the fundamental mode. If a higher order mode is excited in the PS, it will not have the same phase shift as with the fundamental mode because the RI are different for the two modes.

Then we pick the proper W_i for each section. For a taper of width W_i, we calculate the $n_{\text{taper}}(\lambda)$ of the section using FIMMWAVE [34], a commercial simulation software from Photon Design. We simulate a model of waveguide tapered from W_0 to W_i for a length l_0. After getting the phase θ_0 at the end of the taper, we can calculate the effective RI of the taper by $n_{\text{taper}}(\lambda) = \left(\frac{\theta_0}{l_0}\right)\frac{\lambda}{2\pi}$.

Optics EXPRESS

It is worth noting that in FIMMWAVE the simulation only provides the final phase information at the end of the device. We are not able to extract the total phase shift larger than 2π. For that reason we can only simulate a short taper whose optical length is within one wavelength so the phase information of it hasn't been subtracted by $2n\pi$. The problem of simulating such a short taper is that it changes the propagation mode dramatically, which prevent us from comparing a short taper to a longer taper estimated to be hundreds of micrometers in length. The effective RI that we got from the short taper may be inaccurate when applied to a longer one.

To solve this problem, we first simulate the short taper (with length l_{short}) to get a rough effective refractive index $n_{\text{short}}(\lambda)$ which may be slightly different of its counterpart $n_{\text{long}}(\lambda)$ for a longer taper. Then we simulate a long taper whose length l_{long} is hundreds of micrometers, compatible to our estimated taper length. If the simulated phase information of the long taper is θ_{long} ($\theta_{\text{long}}<2\pi$), the total phase shift θ_{shift} should be $\theta_{\text{shift}} = 2n\pi + \theta_{\text{long}}$, where $n = \frac{l_{\text{long}} \cdot n_{\text{short}}(\lambda)}{\lambda}$ (integral part of the wavenumber). So

$$n_{long}(\lambda) = \left(\frac{\theta_{shift}}{l_{long}}\right)\frac{\lambda}{2\pi} = \left(\frac{2\pi\frac{l_{long}\cdot n_{short}(\lambda)}{\lambda} + \theta_{long}}{l_{long}}\right)\frac{\lambda}{2\pi} \tag{4}$$

Combining the simulations of both the short and the long tapers, we can break through the limitation of the simulating software and get the accurate effective refractive index $n_{long}(\lambda)$ for the following design.

We simulate a series of tapers with different taper width W_i to extract their $n_{W_i}(\lambda)$. The difference between W_i and W_0 should not be too large so there will little energy loss through the taper. Around $W_0 = 1\mu m$, we pick W_i to be $0.7\mu m$, $0.8\mu m$ ... $1.3\mu m$. As described above, we fit these $n_{W_i}(\lambda)$ by polynomials to the first and second order separately, corresponding to two- and three-section design.

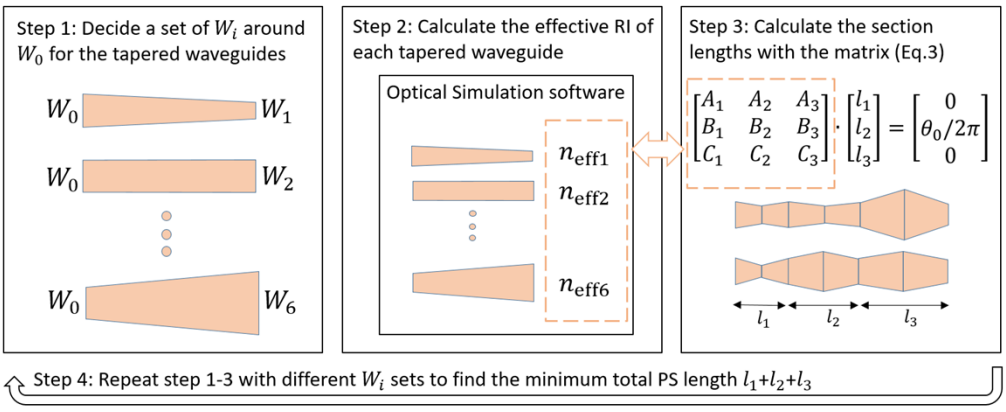

Fig. 7. The workflow to decide the parameters for the shortest TSPS design.

The taper widths of the device should be carefully engineered because the calculated device length can be significantly different for different widths set. We have four taper widths W_1, W_2, W_3, W_4 for the two-section design and six of that for the three-section design. To simplify the engineering problem here, we set $W_2<W_1 = W_3<W_4$ in the two-section design and $W_1<W_2 = W_4<W_3 = W_5<W_6$ in the three-section design. Following the process we discussed above, we calculate and compare the lengths of the sections. The shortest design of the two-section design is given by $W_2 = 0.8\mu m$, $W_1 = W_3 = 1.0\mu m$ and $W_4 = 1.3\mu m$ with the lengths of the sections to be $l_1 = 149.2\mu m$ and $l_2 = 221.9\mu m$. Similarly for the three-section design, we have

Optics EXPRESS

$W_1 = 0.7\mu m$, $W_2 = W_4 = 0.8\mu m$, $W_3 = W_5 = 1.1\mu m$ and $W_6 = 1.3\mu m$ with $l_1 = 970.7\mu m$, $l_2 = 988.4\mu m$ and $l_3 = 1322.7\mu m$. The workflow to decide the parameters is shown in Fig. 7.

We simulate the two arms of the phase shifter separately with the wavelength sweeping from 1450 nm to 1650 nm (shown in Fig. 8(a)). The phase shift $\Delta\theta$ of the TSPS is the phase difference between the output ports of the two arms. Figure 6(d) shows the phase shift of a two-section design as a function of wavelength. The parabolic curve gives about 179° phase shift at 1450 nm, going up to 180.6° around 1550 nm then goes back to 179° at 1650 nm, showing a phase error smaller than 1°.

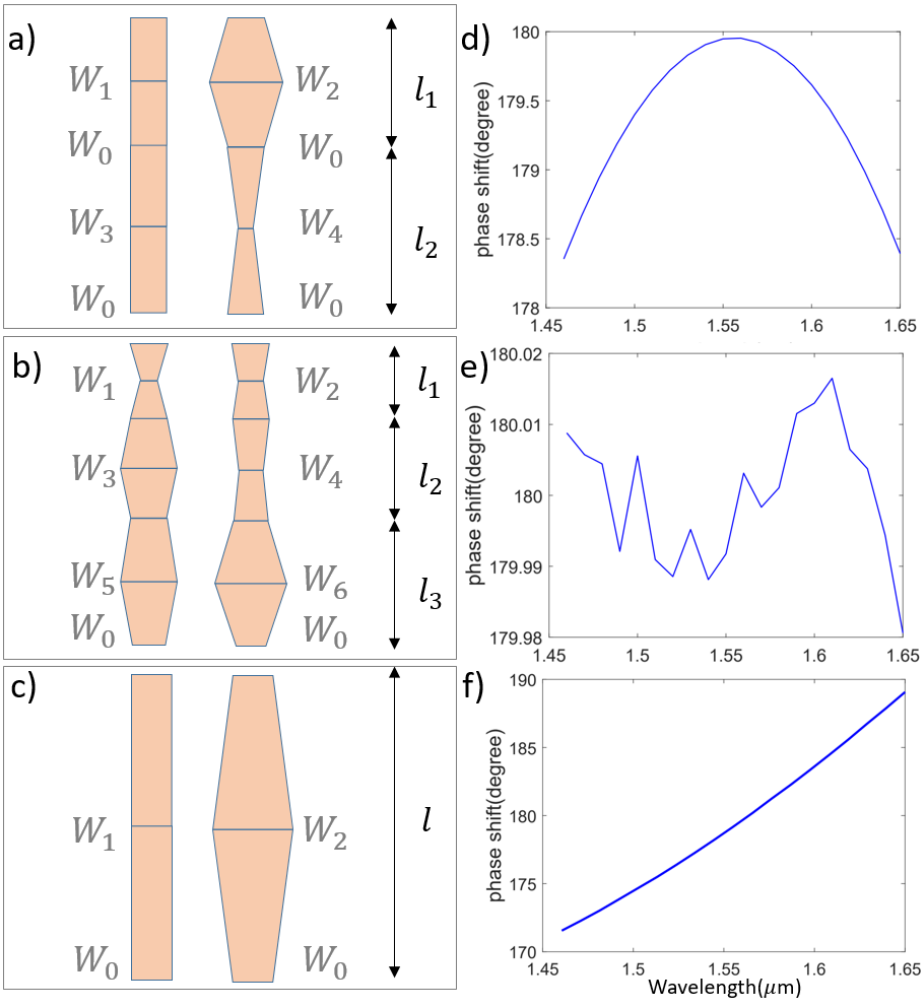

Fig. 8. a, b, c) schematic models of two-section TSPS, three-section TSPS and traditional tapered PS. d, e, f) simulation results of PSs listed above. We show the phase shift value as a function of the wavelength for all three designs. The PSE for two-section TSPS, three-section TSPS and traditional tapered PS are 1°, 0.02° and 9° separately

Furthermore, by fitting the effective RI to the second order to eliminate the dependence of wavelength, the three-section design removes the parabolic characteristic of the phase shift-wavelength curve and reach a phase error less than 0.02° for a 200 nm bandwidth around 1550 nm (see Fig. 8(b), e).

Optics EXPRESS

As a comparison, we have also designed a conventional PS which contains only one section of the paired tapers (see Fig. 8(c)). For the bottom arm the waveguide width tapers up from 1um to 1.2um then tapers back to 1um, with the total length of 69.9um. For the other arm it is a 1um straight waveguide with the same total length. The simulation result shows a phase shift varying from 171° around 1450 nm to 189° around 1650 nm (Fig. 8(f)).

The TSPSs compensate the wavelength dependence of the PS by using multiple sections. The phase error can be reduced from 9° for the conventional PS to 1°/ 0.02° for the two/three-section TSPS.

3.2. Simulation of the broadband MZI

Based on the simulation result of the TSPS, we implement it for the MMI-MZI device (see Fig. 9(a)). The width of the MMI coupler is designed to be 15um so it supports enough numbers of modes as well as has a relatively wide bandwidth. The length of the MMI coupler is optimized to be 166.2um so it performs the best around 1550 nm. Also, the width and offset of the MMI coupler ports have been optimized to be 1.8um and 5.1um, respectively.

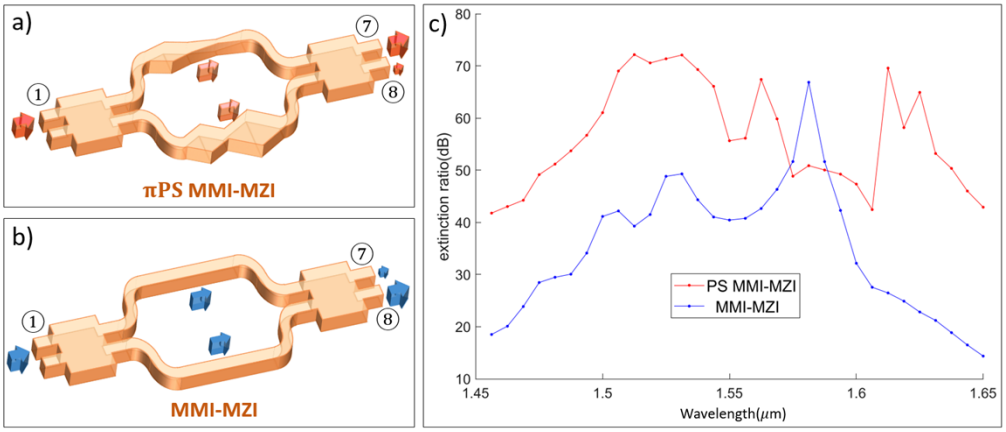

Fig. 9. a, b) Schematic model of πPS MMI-MZI with the TSPS and conventional MMI-MZI. c) Simulated extinction ratio between the two output ports for πPS MMI-MZI (red line) and conventional MMI-MZI (blue line).

To avoid directional coupling between the two arms connecting the cascaded MMI couplers, we increase the separation between them to 16um using a pair of tapered S-bends. We note that we have just increased the separation to 16um for a reasonable simulation speed because the FIMMWAVE calculates the EM field over the entire space. The separation can be larger in the actual fabrication layout. The width of the waveguide is tapered from 1.8um at the MMI coupler output port to 1um so that it supports only the fundamental mode.

Here we choose the two-section TSPS for the compactness of the design. The length of the three-section design is much longer than that of a two-section design, which requires a larger arm separation to avoid the directional coupling effect. The simulation of such a model takes a long time, making optimization and wavelength sweeping nearly impossible.

The simulation result of the π-phase shift MMI-MZI is shown in Fig. 9(c). The extinction ratio (red line) between the two output ports is more than 40 dB from 1450 nm to 1650 nm, while presenting an average value of more than 50 dB.

Compared to the conventional MMI-MZI whose simulation result is shown by the blue line, both the bandwidth and the extinction ratio of the πPS MMI-MZI show obvious improvement, especially for the wavelength on both sides of the shown spectrum, where the extinction ratio is improved by more than 20 dB.

Optics EXPRESS

4. Fabrication

4.1. Experimental characterization and optimization of the broadband phase shifter

The device fabrication is performed on a silicon substrate wafer with a 5um thermal oxide layer. A 300 nm silicon nitride is deposited using low-pressure chemical vapor deposition (LPCVD). The design pattern is written on the positive resist ZEP-520A by e-beam lithography using a 100 kV Elionix ELS G-100 system. A 10 nm chromium layer is deposited after e-beam resist development. The pattern is then transferred to the chromium hard mask with the remaining resist removed by a lift-off process. The silicon nitride is dry etched using an ICP-RIE system and the remaining chromium mask is removed using a Cr wet etching process. Finally, a 5um silicon dioxide cladding is deposited through a plasma enhanced chemical vapor deposition (PECVD) process.

To measure the performance of a phase engineered device such as our taper-section phase shifter, a MZI system is a commonly used tool. If we assume the MZI system to be perfect, the phase information of the two arms can be extracted by measuring the power in the two output ports. The argument is similar to our previous discussion that describes the principle of operation of the πPS MMI-MZI, but this time we consider the phase shift to be an arbitrary angle $\Delta\phi$ and the MMI couplers to be ideal.

As shown in Fig. 10, the amplitude of the mode coming from the port 7 should be:

$$A_7 = \sqrt{\left(\frac{1}{2}\right)^2 + \left(\frac{1}{2}\right)^2 + 2 \cdot \frac{1}{2} \cdot \frac{1}{2} cos(\Delta\phi)} = \sqrt{\frac{1}{2} + \frac{1}{2} cos(\Delta\phi)} \tag{5}$$

$$\text{So the intensity } I_7 = A_7^2 = \frac{1}{2} + \frac{1}{2}\cos(\Delta\phi) = sin^2\left(\frac{\Delta\phi}{2}\right) \tag{6}$$

$$\text{Similarly for the port 8 the intensity } I_8 = cos^2\left(\frac{\Delta\phi}{2}\right) \tag{7}$$

$$\text{The extinction ratio is } ER = tan^2\left(\frac{\Delta\phi}{2}\right) \tag{8}$$

$$\text{So the phase shift can be estimated by } \Delta\phi = 2\sqrt{\tan^{-1}(ER)} \tag{9}$$

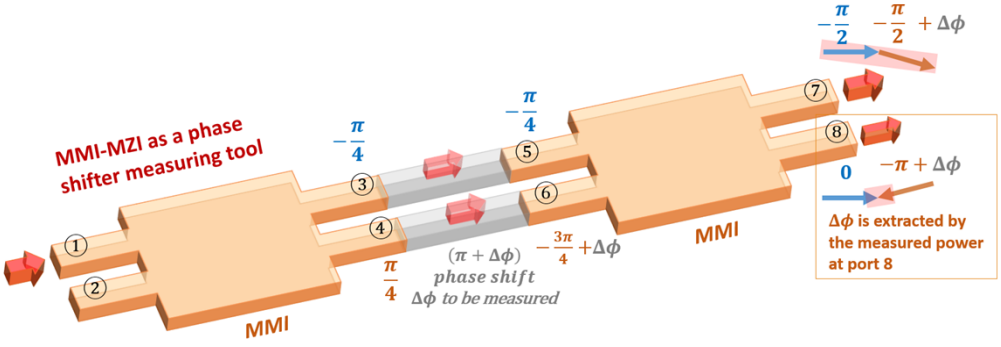

Fig. 10. MMI-MZI as a tool to measure the PSE when the optical component in the MZI arms is the main source of phase error. Here the errors in the MMI can be ignored comparatively.

For a phase engineering device whose phase error is as large as several degrees, the phase inaccuracy of the MMI coupler is relatively small so that it can be ignored. However for our TSPS

Optics EXPRESS

which targets a very small phase error, the MMI phase error will influence the measurement and the characterization.

To address this problem, we connect multiple πPSs to amplify its phase error. So it can be the dominant phase error source in the MZI. As shown in Fig. 11, we connect seven identical πPSs to form a 7π PS which should function similarly to a single πPS. The difference is that the PSE will be amplified by seven times so it will be easier to be accounted by the output power measurement. Also the phase inaccuracy of the MMI coupler become insignificant again compared to the amplified PSE.

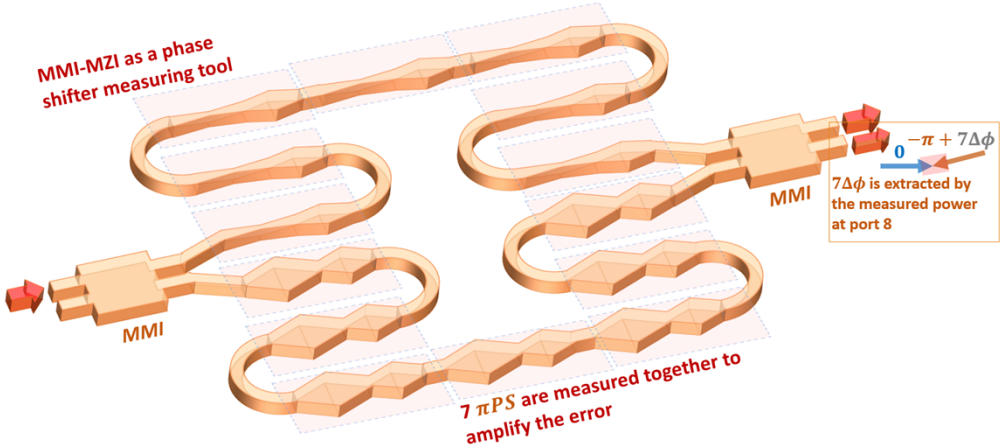

Fig. 11. The schematic model of the 7π PS MMI-MZI. The cascaded PSs are circled by red squares. The phase errors of 7 π-phase shifters accumulate so the error from MMI-MZI can be ignored comparatively.

We note that, although the energy drops for both ports if the MMI coupler operates away from its designed wavelength, the relationship between the phase shift and the extinction ratio in Eq. (9) still holds. The energy of two MMI coupler output ports decreases simultaneously when the wavelength shifts away from the center wavelength. The extinction ratio remains the same as long as the power splitting of the MMI is still balanced.

The total length of this 7π PS is seven times the single πPS length if we connect those πPSs end to end directly. That will increase the strength of directional coupling between the two arms. To control the length of this 7π PS, we use several 180° bends to rearrange the positions of the πPSs as shown in Fig. 11. The radius of the bends is set to be 100um so the bending loss is negligible, also the separation between the parallel waveguides can be 200um, which is sufficiently large to prevent directional coupling.

Since the RI of the waveguide is sensitive to its width, a small bias in the fabrication process will cause the difference between the simulation and experimental results. For the optimization convenience, here we choose the two-section TSPS in our design. As discussed before, we have: $\frac{\theta(\lambda)}{2\pi} = \frac{(A_1 l_1 + A_2 l_2)}{\lambda} + (B_1 l_1 + B_2 l_2)$. If $A_{1,2}, B_{1,2}$ in the actual device are different from the theoretical number, the trend of the phase-wavelength curve may not be flat.

$\theta(\lambda)$ increases as λ increases, if $A_1 l_1 + A_2 l_2 < 0$. And it decreases as λ increases, if $A_1 l_1 + A_2 l_2 > 0$. Now that $A_1 > 0 > A_2$, we can increase l_1/l_2 if $A_1 l_1 + A_2 l_2 < 0$ or decrease l_1/l_2 if $A_1 l_1 + A_2 l_2 > 0$ to get $A_1 l_1 + A_2 l_2 \approx 0$. Then we can scale l_1, l_2 with a same factor so the total phase shift can be adjusted without changing the l_1, l_2 ratio that we have optimized. In that way we are able to optimize the design according to the measured results experimentally. On the other hand, the relationship between the phase-wavelength curve and the section lengths of the three TSPS is

Optics EXPRESS

less straightforward. Although the performance of it is better than the two-sections design, the parameter optimization of three sections can be too complicated.

Additionally, since our device is designed for TE modes, a TM filter consisting of a set of 90-degree bends with a radius of 50μm has been added to reduce TM noise. By leveraging the different bending losses of the fundamental TE and TM modes, the TM noise can be effectively suppressed while the TE mode experiences minimal loss.

As a comparison, we also fabricate a 7π PS using a conventional πPSs using the design in section 3.1(Fig. 8(c)). To measure the performance of these 7π PSs, the optical chip is butt coupled to a TE polarized tunable laser source Keysight 8164B LMS Mainframe/81600B tunable laser source with a tuning bandwidth of 1450nm-1640 nm. The output spectrum of our device is then measured using a Keysight N7744A detector.

Figure 12 shows the normalized transmission spectrum for the optimized devices. Figure 12(a) shows the transmission curves of two MZI output ports when the conventional 7π PS is applied. The extinction ratio reaches its peak around 1563 nm, indicating that the phase shift between the two arms is about π ($or\ \pi + 6\pi$). The extinction ratio drops when the two curves gets closer at 1460 nm as well as 1640 nm, indicating the phase shift goes close to $\frac{\pi}{2}$, $\frac{3\pi}{2}$ $\left(or \frac{\pi}{2}, \frac{3\pi}{2} + 6\pi\right)$ for these shorter and longer wavelengths. This shows the strong wavelength dependence of the conventional PS.

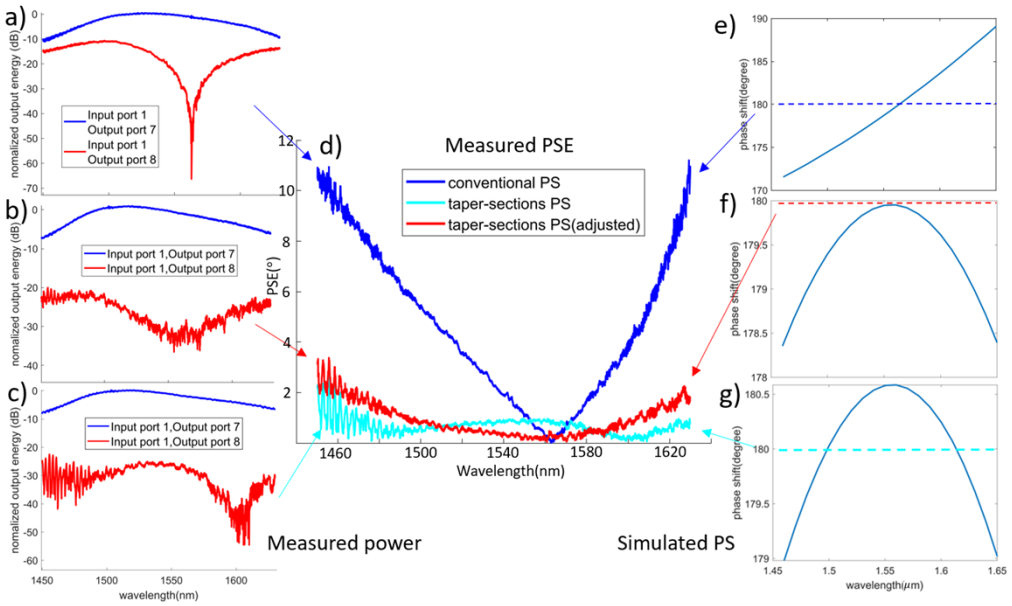

Fig. 12. Measured power from two MZI output ports with a) conventional tapered PS, b)adjusted two-section TSPS, c) two-section TSPS inserted into the MZI arms (the device in Fig. 11). d) PSE of these three PSs extracted from the measured MZI output power in insets a, b and c. To note, here PSE is the difference between the actual phase shift and the desired 180°. e, f, g) simulation results of these three PSs as a comparison, with dotted lines showing the level where PSE equals to zero (when the phase shift is 180°).

Based on the relationship between the PSE and the extinction ratio (Eq. (9)), we plot the PSE as a function of wavelength (Fig. 12(d)). The measured PSE for the conventional PS (blue line) is about 12° when it deviates from the center wavelength. The PSE of the TSPS (red line) is about 1° for a 180 nm bandwidth. In addition, we present an adjusted TSPS (cyan line) that has a PSE smaller than 0.6° for a 90 nm bandwidth. This adjustment is realized by shrinking the total

Optics EXPRESS

length of the PS slightly so the peak of the parabolic curve (see figure) decreases to 180°. Such an adjusted TSPS can be used in the case where the phase error requirement is stricter within a relatively narrow bandwidth.

4.2. Experimental realization of the broadband MZI

After optimizing the TSPS, we move to the 7π back to the πPS to measure the performance of the πPS MMI-MZI. As a comparison, we also fabricated the conventional MMI-MZI.

As shown in Fig. 13(c) (red line), the extinction ratio of the πPS MMI-MZI is around 40 dB from 1500 nm to 1600 nm, dropping to around 25 dB for shorter wavelength at 1450 nm and to around 35 dB for longer wavelength at 1650 nm. Compared to the conventional MMI-MZI (blue line) there is an obvious improvement for the extinction ratio especially for the two sides of the inspected band.

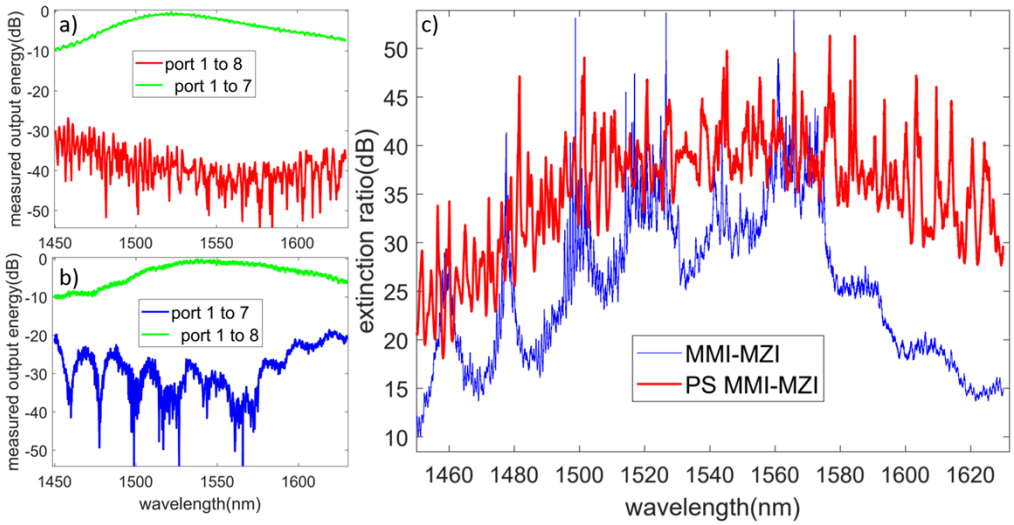

Fig. 13. a, b) Measured output power for πPS MMI-MZI (Fig. 9(a)) and MMI-MZI (Fig. 9(b)) c) Extinction ratio for πPS MMI-MZI (in red) and MMI-MZI (in blue). A significant improvement of extinction ratio and bandwidth can be observed (corresponding to the simulations in Fig. 9(c)).

5. Conclusions

In conclusion, we have designed a πPS MMI-MZI to compensate the power imbalance and phase inaccuracy brought by the imperfection and bandwidth limitation of the MMI couplers, using an innovative broadband taper-section phase shifter (TSPS). The simulations on FIMMWAVE predict an unprecedented PSE of 1° and 0.02° for a two- and three-section design, respectively. Applying this broadband TSPS to the πPS MMI-MZI, the simulation shows an extinction ratio of about 50 dB over a 150 nm bandwidth, compared to 30 dB for the conventional MMI-MZI. After experimental optimization, the PSE of the TSPS is measured to be around 1° from 1450 nm to 1650 nm. In addition, an adjusted TSPS gives a 0.6° PSE for a narrower bandwidth of around 90 nm. Applying our broadband PS, the extinction ratio of the πPS MMI-MZI is measured to be 40 dB for a 100 nm bandwidth, which is a significant improvement compared to the conventional MMI-MZI which has an extinction ratio of 30 dB for 90 nm bandwidth. Our low PSE broadband TSPS, as well as the broadband MMI-MZI, can serve as valuable components in broadband

Optics EXPRESS

integrated photonic circuits; they promise to have wide applications in astrophotonics, sensing, spectroscopy and quantum photonics.

Funding. National Aeronautics and Space Administration (NASA # 21-APRA21-0116).

Disclosures. The authors declare no conflicts of interest.

Data availability. Data underlying the results presented in this paper are not publicly available at this time but may be obtained from the authors upon reasonable request.

References

1. M.-A. Martinod, B. Norris, P. Tuthill, *et al.*, "Scalable photonic-based nulling interferometry with the dispersed multi-baseline GLINT instrument," Nat. Commun. **12**(1), 2465 (2021).
2. B. R. Norris, N. Cvetojevic, T. Lagadec, *et al.*, "First on-sky demonstration of an integrated-photonic nulling interferometer: the GLINT instrument," Mon. Not. R. Astron. Soc. **491**(3), 4180–4193 (2020).
3. H. Xu and Y. Shi, "Flat-top CWDM (de) multiplexer based on MZI with bent directional couplers," IEEE Photonics Technol. Lett. **30**(2), 169–172 (2018).
4. M. He, M. Xu, Y. Ren, *et al.*, "High-performance hybrid silicon and lithium niobate Mach–Zehnder modulators for 100 Gbit s− 1 and beyond," Nat. Photonics **13**(5), 359–364 (2019).
5. A. Rao, G. Moille, X. Lu, *et al.*, "Up to 50 dB extinction in broadband single-stage thermo-optic Mach-Zehnder interferometers for programmable low-loss silicon nitride photonic circuits," in *CLEO: Science and Innovations* (Optica Publishing Group, 2021), SM1A. 7.
6. I. Zand and W. Bogaerts, "Effects of coupling and phase imperfections in programmable photonic hexagonal waveguide meshes," Photonics Res. **8**(2), 211–218 (2020).
7. X. Qiang, X. Zhou, J. Wang, *et al.*, "Large-scale silicon quantum photonics implementing arbitrary two-qubit processing," Nat. Photonics **12**(9), 534–539 (2018).
8. C. M. Wilkes, X. Qiang, J. Wang, *et al.*, "60 dB high-extinction auto-configured Mach–Zehnder interferometer," Opt. Lett. **41**(22), 5318–5321 (2016).
9. M. Jin, J.-Y. Chen, Y. M. Sua, *et al.*, "High-extinction electro-optic modulation on lithium niobate thin film," Opt. Lett. **44**(5), 1265–1268 (2019).
10. S. Liu, H. Cai, C. DeRose, *et al.*, "High speed ultra-broadband amplitude modulators with ultrahigh extinction> 65 dB," Opt. Express **25**(10), 11254–11264 (2017).
11. S. Xie, S. Veilleux, and M. Dagenais, "On-chip high extinction ratio single-stage Mach-Zehnder interferometer based on multimode interferometer," IEEE Photonics J. **14**(6), 1–11 (2022).
12. G. Reed, G. Mashanovich, F. Gardes, *et al.*, "Silicon optical modulators," Nat. Photonics **4**(8), 518–526 (2010).
13. Y. Li, C. Li, C. Li, *et al.*, "Compact two-mode (de) multiplexer based on symmetric Y-junction and multimode interference waveguides," Opt. Express **22**(5), 5781–5786 (2014).
14. D. González-Andrade, A. Dias, J. G. Wangüemert-Pérez, *et al.*, "Experimental demonstration of a broadband mode converter and multiplexer based on subwavelength grating waveguides," Opt. Laser Technol. **129**, 106297 (2020).
15. J. Van Campenhout, W. M. Green, S. Assefa, *et al.*, "Low-power, 2× 2 silicon electro-optic switch with 110-nm bandwidth for broadband reconfigurable optical networks," Opt. Express **17**(26), 24020–24029 (2009).
16. Y. Xiong, R. B. Priti, and O. Liboiron-Ladouceur, "High-speed two-mode switch for mode-division multiplexing optical networks," Optica **4**(9), 1098–1102 (2017).
17. S. S. Djordjevic, L. W. Luo, S. Ibrahim, *et al.*, "Fully reconfigurable silicon photonic lattice filters with four cascaded unit cells," IEEE Photonics Technol. Lett. **23**(1), 42–44 (2011).
18. P. Orlandi, C. Ferrari, M. J. Strain, *et al.*, "Reconfigurable silicon filter with continuous bandwidth tunability," Opt. Lett. **37**(17), 3669–3671 (2012).
19. N. C. Harris, Y. Ma, J. Mower, *et al.*, "Efficient, compact and low loss thermo-optic phase shifter in silicon," Opt. Express **22**(9), 10487–10493 (2014).
20. M. Poot and H. X. Tang, "Broadband nanoelectromechanical phase shifting of light on a chip," Appl. Phys. Lett. **104**(6), 061101 (2014).
21. L. McKay, M. Merklein, A. C. Bedoya, *et al.*, "Brillouin-based phase shifter in a silicon waveguide," Optica **6**(7), 907–913 (2019).
22. M. Burla, L. R. Cortés, M. Li, *et al.*, "On-chip programmable ultra-wideband microwave photonic phase shifter and true time delay unit," Opt. Lett. **39**(21), 6181–6184 (2014).
23. Q. Chang, Q. Li, Z. Zhang, *et al.*, "A tunable broadband photonic RF phase shifter based on a silicon microring resonator," IEEE Photonics Technol. Lett. **21**(1), 60–62 (2009).
24. D. González-Andrade, J. G. Wangüemert-Pérez, A. V. Velasco, *et al.*, "Ultra-broadband mode converter and multiplexer based on sub-wavelength structures," IEEE Photonics J. **10**(2), 1–10 (2018).
25. S. Yegnanarayanan, P. Trinh, F. Coppinger, *et al.*, "Compact silicon-based integrated optic time delays," IEEE Photonics Technol. Lett. **9**(5), 634–635 (1997).
26. A. Herrero-Bermello, A. V. Velasco, H. Podmore, *et al.*, "Temperature dependence mitigation in stationary Fourier-transform on-chip spectrometers," Opt. Lett. **42**(11), 2239–2242 (2017).

Optics EXPRESS

27. P. Morrissey and F. Peters, "Multimode interference couplers as compact and robust static optical phase shifters," Opt. Commun. **345**, 1–5 (2015).
28. L. Han, S. Liang, H. Zhu, *et al.*, "Two-mode de/multiplexer based on multimode interference couplers with a tilted joint as phase shifter," Opt. Lett. **40**(4), 518–521 (2015).
29. D. González-Andrade, J. M. Luque-González, J. G. Wangüemert-Pérez, *et al.*, "Ultra-broadband nanophotonic phase shifter based on subwavelength metamaterial waveguides," Photonics Res. **8**(3), 359–367 (2020).
30. T. Klinner-Teo, M.-A. Martinod, P. Tuthill, *et al.*, "Achromatic design of a photonic tricoupler and phase shifter for broadband nulling interferometry," J. Astron. Telesc. Instrum. Syst. **8**(4), 045001 (2022).
31. L. B. Soldano and E. C. Pennings, "Optical multi-mode interference devices based on self-imaging: principles and applications," J. Lightwave Technol. **13**(4), 615–627 (1995).
32. X. Ai, Y. Zhang, W.-L. Hsu, *et al.*, "Broadband 2× 2 multimode-interference coupler on the silicon-nitride platform," Opt. Express **32**(6), 9405–9419 (2024).
33. P. Labeye, "Composants optiques intégrés pour l'interférométrie astronomique," (Institut National Polytechnique de Grenoble-INPG, 2008).
34. https://www.photond.com.